Development of thermal barrier coating systems from Al microparticles – Part II: Characterisation of mechanical and thermal transport properties

Germain Boissonnet*, Jean-Luc Grosseau-Poussard, Gilles Bonnet, Fernando Pedraza

Laboratoire des Sciences de l'Ingénieur pour l'Environnement – Université de La Rochelle

LaSIE, UMR-CNRS 7356, Avenue Michel Crépeau, 17042 La Rochelle Cedex 1, France

* Corresponding author: germain.boissonnet@univ-lr.fr

Abstract

Keywords: slurry coating; thermal barrier coating; thermal diffusivity; scratch tests

1. Introduction

Finding alternative coating technologies to the standard thermal barrier coatings (TBCs) to extend the protection to the lower stages of the turbine is of growing interest as current technologies implies expensive and complex processes. As demand for efficiency and reduction of fuel consumption and greenhouse gas emission is a mandatory concern for the future design of gas turbine engines, the temperature will thus rise in low pressure turbine (LPT) section as well. Among the different options, the formation of a complete thermal barrier coating using the slurry technique appears to be a convincing alternative for the protection of materials

of this LPT section due to its relative low cost and ease of application [1]. This technology uses an aqueous slurry that contains Al microparticles which form, after a proper annealing, a foam of hollow alumina microspheres on top of an aluminide coating [1–7]. In a previous study, the resulting 40 μm-thick foam coating was shown to confer equivalent insulative properties than those of a conventional 400 μm YSZ TBC deposited by plasma spray [8]. However, this light foam coating was also observed to be particularly brittle and not sufficiently resistant to be a convincing solution. Therefore, in the first part of this work which was published earlier, the goal was to improve the mechanical strength of the top foams by controlling the atmosphere of the annealing in order to promote the growth of the oxide shells of the original microparticles while enabling enough Al to react with the Ni substrate to form the diffusion coating [2]. In this previous study, the authors investigated the influence of Ar, synthetic air, water vapour as well as hybrid atmosphere on the mechanisms of coating formation and showed that different microstructures were achieved. While a fast consumption of Al occurred in inert Ar atmosphere to form the aluminides, synthetic air and water vapour promoted the strengthening of the microparticles oxide shell but also hampered the diffusion of the Al toward the substrate resulting in heterogeneous aluminide coatings. Hybrid treatments allowed compromises between the thickening of the shells and the providing of Al for the diffusion coating by delaying the introduction of the oxidizing atmosphere. The different annealing in single and hybrid atmospheres resulted in various microstructures of the coating systems with, for instance, different top foam and oxide shell thickness, homogeneity of the aluminide and the presence of oxide and un-emptied Al microparticles in the top coating.

However, the mechanical strength, adhesion and thermal insulation properties were not investigated in this previous study as it mostly focused on the coating formation mechanisms. Therefore, this work aims at filling this purpose to evaluate the relevance and applicability of such coatings.

2. Experimental procedure

2.1. Materials and microstructural characterization

The coatings were performed on pure Ni (99.98% purity, Goodfellow) discs samples of 12.7 mm diameter. The coatings were achieved by the heat treatment of slurries made from Al micro-sized particles that were previously sprayed on the surface of the Ni substrates. Two different types of Al powders were used: ones with a homogeneous size distribution and that possessed a slightly thicker passive shell (**HS**), and others of a more dispersed size distribution with thin passive shells (**DS**). After the deposition of the slurry (approximately 9±1 $mg \cdot cm^{-2}$), the samples were dried in a fume cupboard for 1h and, annealed in a thermobalance following a three-step heating program. With heating ramps fixed at $5°C \cdot min^{-1}$, the samples were first cured at 400°C to remove the organic binder (polyvinyl alcohol), then heated at 700°C for 2h to allow the Al to melt and to diffuse into the substrate, and finally annealed at 1100°C for 2h to stabilise the oxide into α-Al_2O_3 and the diffusion coating into a β-NiAl phase. The thermal treatments were conducted into different atmospheres to optimize the thickening of the shells by oxidizing the leaking Al coming out of the micro-sized particles while allowing enough Al to reach the substrate for the aluminisation to occur. For this purpose, Ar and synthetic air were employed to perform the thermal treatments. Moreover, hybrid atmosphere heat treatments were investigated where the Ar was replaced with synthetic air at different temperature of the annealing during the heating ramp from 400°C to 700°C. The **Table 1** shows a summary of the samples with the different annealing performed.

Table 1 – Summary of the different heat treatments performed in TGA.

Type of Al microparticles	Heat treatment	Starting atmosphere	Introduction of synth. air	Sample ID
DS	400°C-1h	Ar	-	DS-Ar / HS-Ar

(dispersed size)	+700°C-2h	Synthetic air		DS-air / HS-air
or	+1100°C-2h	Ar	550°C	DS-550 / HS-550
HS			600°C	DS-600 / HS-600
(homogeneous size)			650°C	DS-650 / HS-650
			700°C	DS-700 / HS-700

The analysis of surfaces and cross sections of the samples were carried out using scanning electron microscopy (SEM FEI Quanta 200F) coupled to an energy dispersive x-ray spectroscopy detector (EDS EDAX) for elemental analysis. Each sample was mounted in an epoxy resin and cross sections were polished till a fineness of 1 μm using 1μ diamond paste (Nap B1 STRUERS).

2.2. Scratch tests and micro-indentation

Micro-indentation was performed in order to assess the hardness of the coatings of the study and to compare them with standard thermal barrier coatings made by plasma-spray or EB-PVD that are presented in other studies [9,10]. The normal force applied for the penetration of Vickers indents was recorded as a function of the depth of penetration till reaching 5 μm into the coating. This depth was chosen in accordance with the different thickness of the measured coatings.

While micro-indentation is the common method to measure the hardness of the coatings, the scratch test is a well-known technique that is used to assess the coating/substrate adhesion of thin hard coating on different types of substrates [11]. This adhesion is measured from an indent that is drawn across the coated surface with an increasing load until a defined failure occurs at a load known as the critical load, L_C. Depending on multiple factors that are usually reduced to the hardness of both substrate and coating, different modes of failures that include coating detachment, through-thickness cracking, plastic deformation or cracking in the coating or substrate may occur during the scratch test. Therefore, the adherence of the TBCs made from the slurry route was appraised using the scratch test method. Scratching experiments were performed using a scratch tester (ANTON-PARR STEP E400) with a Rockwell-M-120 diamond indenter with a 100 μm tip radius coupled to

an acoustic emission sensor. The range load was set to 0.03 to 10 N over a length of 5 mm with a speed rate of 2.5 mm·min^{-1} and an acquisition rate of 30 Hz.

One shall note that a prescan at 0.03 N was performed prior to each scratch or micro-indentation test to identify the original surface of the sample and thus, was already damageable to the weakest coatings as it could already penetrate them. Therefore, the measured depth must be considered carefully. Additional indentation at 0.03 N using the same indenter were performed on the different coatings to assess the impact of the prescan.

2.3. Thermal insulation assessment

While the thermal conductivity (λ) is usually employed in the literature to describe the thermal insulation potential of thermal barrier coatings, it is derived from the thermal diffusivity (α), the density (ρ) and the specific heat capacity (C_p) following the equation 1:

$$\lambda(T) = \alpha(T) \times \rho(T) \times C_p(T) \quad (1)$$

However, as the coatings present various porous microstructures, it is very complex to measure the specific heat capacity or the density of the coatings with the precision needed to calculate the true thermal conductivity. Therefore, as stated in other studies, it is often preferable to discuss the thermal diffusivity of the coatings in a comparative manner to assess the thermal insulation potential of such coatings. The high-temperature thermal diffusivity was determined using a laser-flash apparatus (LFA 1600 LINSEIS) working under vacuum (~1.10^{-2} mbar) with the measurements being made every 100°C from room temperature till 1100°C. Prior to the laser-flash measurements, the thickness of the samples was assessed using a digital calliper (±10^{-3}) and both surfaces of the disc samples were coated with a 4-5 um graphite layer to increase absorption of the laser pulse on the back side as well as the emissivity of the heat signal on the front side to be measured with the InSb infrared detector. For post-processing multi-layer calculations (2-layer model) in order to extract the

contribution of the coating, the thickness of each layer was measured from the cross-section images.

3. Results

3.1. Microstructure of the thermal barrier systems

The **Figure 1** and **Figure 2** gathers respectively the surfaces and the cross sections of the coatings that were synthesized using the different atmospheres. As expected, the different atmospheres resulted in a wide variety of coating microstructures due to the difference in type of Al microparticles and oxidation potential that depend on the duration of the exposition to the synthetic air (full Ar < air introduced at 700°C < 650°C < 600°C < 550°C < full synthetic air).

In Ar atmosphere, both DS and HS microparticles resulted in thin top coatings made of the collapsed hollow particles, i.e. ~8 μm for DS-Ar and ~20 μm for HS-Ar (**a** and **f** from **Figures 1** and **2**). The dark grey aspect of the coating heat treated under Ar in **Figure 1** results from the poor oxidation of the top coatings, i.e. the hollow microparticles have such thin shells that it is possible to see the substrate colour through. In synthetic air, the aspect is also grey due to the presence of metallic Al trapped in some of the particles (see **e** and **f** from **Figures 1** and **2**). In air, the resulting top coatings are thick due to the early oxidation of the particles, i.e. ~60 μm for DS-air and ~50 μm for HS-air, but the diffusion coatings obtained are heterogeneous and display a NiO layer on top of a thick alumina layer. By modifying the temperature of introduction of synthetic air as a replacement of the Ar atmosphere during the heat treatment, various structures were achieved. Introducing the synthetic air at 600°C led to the important oxidation of the coatings. However, in contrast with the complete heat treatment under synthetic air, the switch led to spallation of the top coating for the HS-600 sample (**Figure 1d** and **2d**) and to cracks and voids at the interface between the diffusion coating and the top coating for the

DS-600 sample (**Figure 2i**). With further delaying of the introduction of air, homogeneous diffusion coatings were achieved with thicker top coatings than the ones obtained with pure Ar atmosphere, i.e. ~40, ~35, ~30 and ~15 µm for HS-650, HS-700, DS-650, and DS-700 respectively (**Figure 2c**, **2b**, **2h** and **2g**).

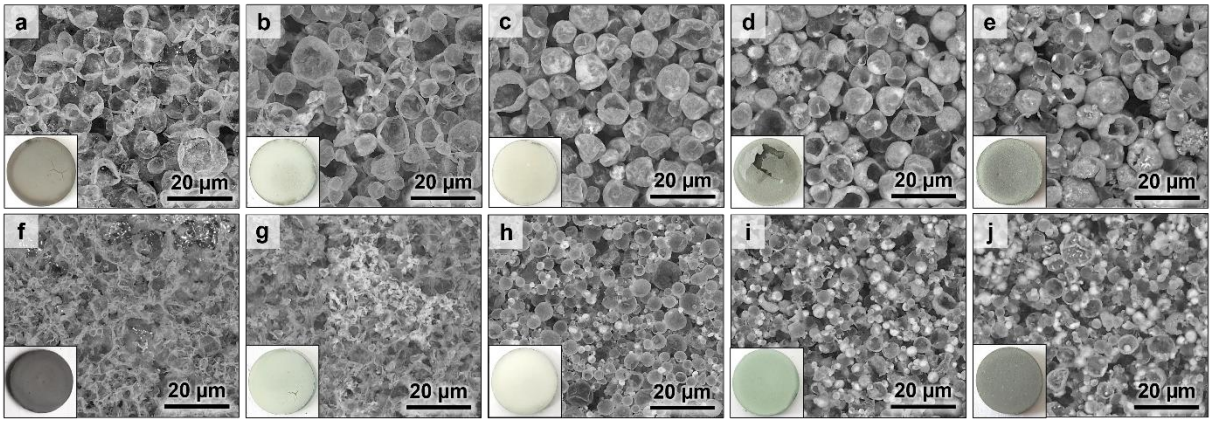

Figure 1 – SEM surfaces of the coatings of the study; a) HS-Ar, b) HS-700, c) HS-650, d) HS-600, e) HS-air, f) DS-Ar, g) DS-700, h) DS-650, i) DS-600 and j) DS-air.

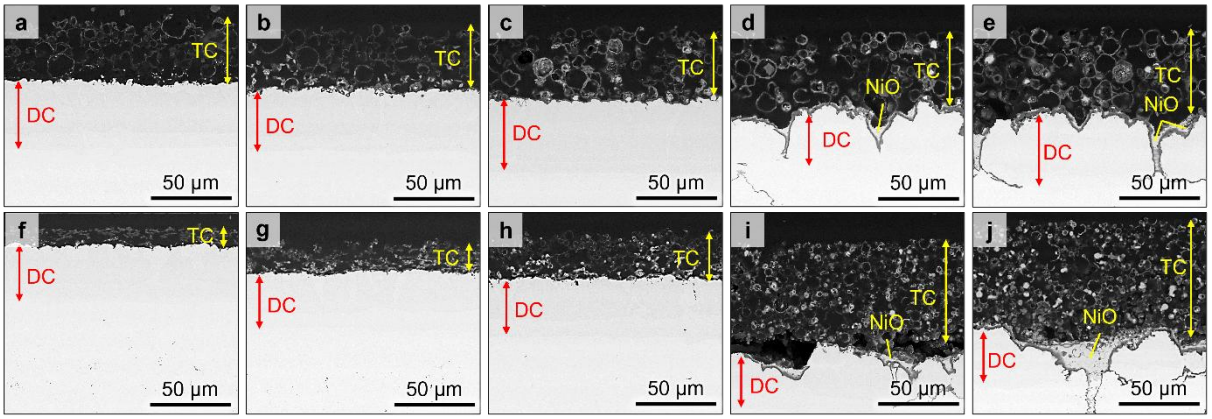

Figure 2 – SEM cross-sections of the coatings of the study; a) HS-Ar, b) HS-700, c) HS-650, d) HS-600, e) HS-air, f) DS-Ar, g) DS-700, h) DS-650, i) DS-600 and j) DS-air.

To highlight the impact of the increasing oxidation potential of the different heat treatment, top coating thickness as well as the thickness of the shell of the emptied microparticles were also plotted for the different samples on **Figure 3** and **Figure 4** respectively. For both types of microparticles, the top coating thickness as well as the thickness of the walls from the microspheres tend to increase with greater exposition to the synthetic air during the heat treatment. **Figure 3** shows that the oxide shell of the HS particles is greater than the DS ones for all the different heat treatment while

the growth rate of both particles is similar with respect to the increase of exposure to synthetic air. However, the top coating thickness evolution displayed in **Figure 4** shows very different behaviour between the two types of particles. While the HS microparticles lead to the slow growth of the coating thickness, the DS microparticles show an abrupt increase in the growth of the top coating when considering the two samples in the most oxidizing heat treatment (with air introduced at 600°C and in the full synthetic air atmosphere).

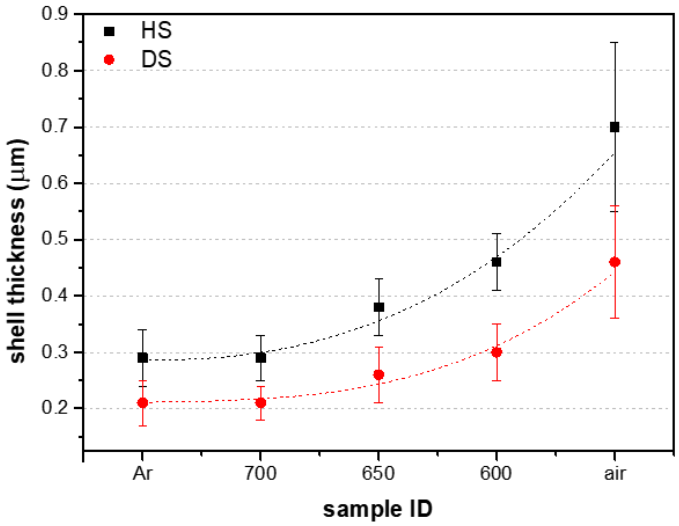

Figure 3 **–** **S**hell thickness of the samples top coatings measured using SEM micrographs.

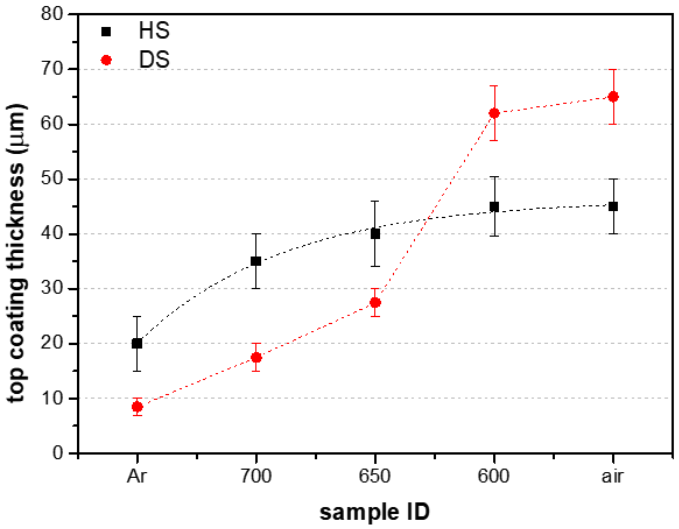

Figure 4 – Top coating thickness of the samples measured using SEM micrographs.

3.2. Mechanical tests

Figure 5 shows the penetration depth of the indent as a function of the applied force across the length of the scratch line while **Table 2** gathers the penetration depth measured in different locations. As the coating of the HS-600 sample had already spalled from the surface, no scratch was performed on its surface. Similarly, only the coating of the DS-600 samples spalled during the scratch test (see also **Figure 6**). This is observed on the **Figure 5b** as a sharp drop of the penetration depth was registered in the early stage of the scratch. All the other coatings remained adherent to the underlying coating after the scratch tests. The recorded depths against the applied load (**Figure 5**) follows a two-stage sequence: (*1*) Over the first microns of the scratch, the indent tends to penetrate the whole thickness of the coatings as highlighted by the early drop of the measured depth. The maximum penetrated depth (D_{max} in **Table 2**) appears to be similar and, in some cases, even higher than the thickness of the top coatings of the different samples. Moreover, the measured depth at 0.5 N ($D_{0.5N}$ in **Table 2**) corresponds to values close to the total coating thickness. As mentioned in **§2.2,** it is necessary to acknowledge the contribution of the prescan that was performed at 0.03 N (see **Figure 6b**). As a matter of fact, the coating depth penetrated with only 0.03 N ($D_{0.03N}$ on **Table 2**) shows that the penetration of the indent is already quite significant compared to the coating thickness and thus, this $D_{0.03N}$ value should be added to the D_{max} and $D_{0.5N}$ depths to obtain the effective penetrated depth. It is also observed that the $D_{0.03N}$ tends to decrease as the top coatings are more oxidized (700 < 650 < air). In contrast, the coatings annealed in Ar exhibit smaller penetration at 0.03 N as coating thicknesses are in the same range as the penetrated depth. In addition, for the most oxidised and thickest coatings, the measured depth follows a stable stage after the sharp drop until a given value of applied force is reached. (*2*) Afterwards, the penetration of the indent tends to stabilize and steadily increases as it starts to reach the diffusion coating. The **Figure 6** shows an example of a scratch that was observed by SEM. Except for the DS-600

sample where the coating completely detached from the substrate, every scratch performed looks like the one presented for DS-650 sample in **Figure 6c**. As the micrograph from **Figure 6b** shows, the indenter penetrates and reaches the substrate surface (the aluminide coating) in the early stage of the scratch where the applied force is less than 0.5 N.

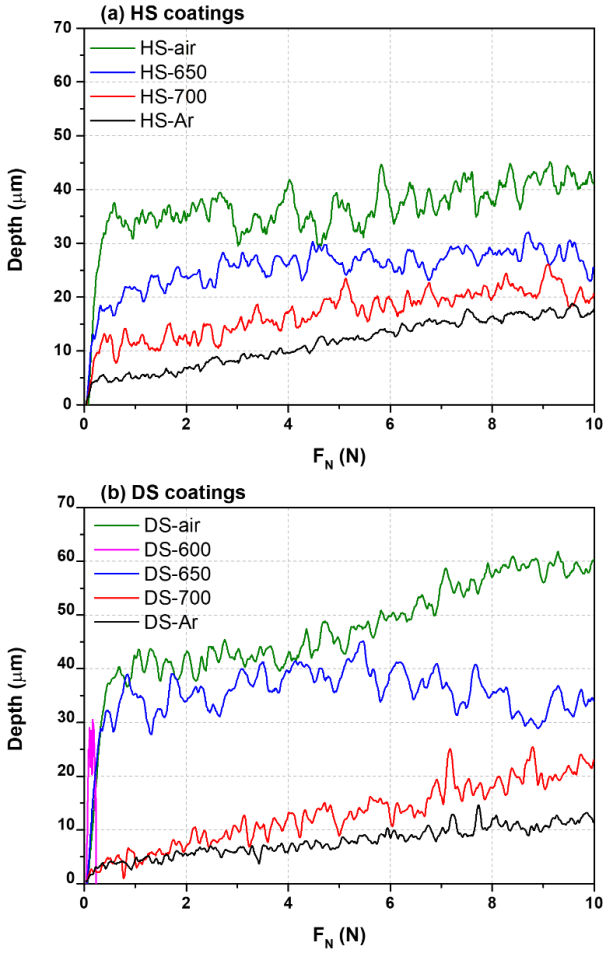

Figure 5 – Depth as a function of the applied load F_N during scratch tests.

Table 2 –Depth of penetration measured after the scratch tests. D_{max} and $D_{0.5N}$ correspond to the maximum depth and the depth reached at 0.5 N of applied force respectively. $D_{0.03N}$* was measured using additional indentations at 0.03 N.

Atmosphere of heat treatment	**D_{max} (μm)**		**$D_{0.5N}$ (μm)**		**$D_{0.03N}$* (μm)**	
	HS	DS	HS	DS	HS	DS
Ar	19.0	14.7	4.5	3.9	5.9 ± 1.4	6.5 ± 2.4
Switch 700°C	23.4	25.7	10.2	4.8	11.0 ± 5.0	8.1 ± 1.1

Switch 650°C	32.2	45.2	18.6	32.4	9.3 ± 6.3	4.8 ± 0.9
Switch 600°C	-	30.6	-	-	-	-
Synthetic air	44.5	61.9	36.8	40.3	5.5 ± 2.2	5.9 ± 3.4

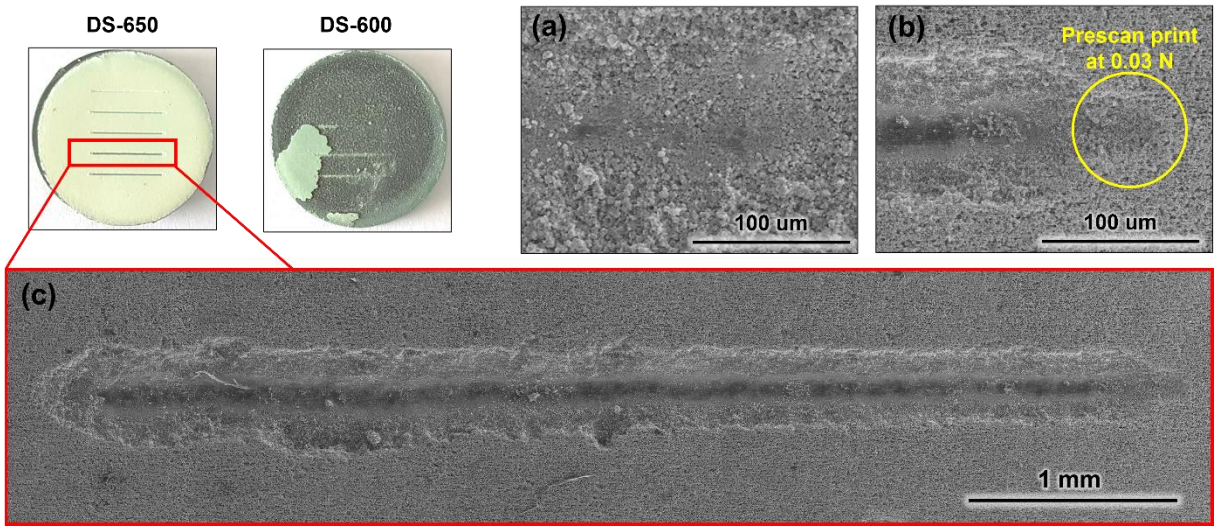

Figure 6 – Macrographs of DS-650 and 600 after the scratch tests and corresponding SEM micrographs in SE mode of a) the bottom of the scratch, b) the beginning of the scratch and c) the scratch in full length.

In addition, the **Figure 6c** shows no evidence of large spallation of the coating around the scratch. As these observations are the same for the different scratches of the coatings, at the exception of the DS-600 sample that lost its coating after the scratch and of the HS-600 sample where the coating was already detached from the substrate, this means that the adhesion strength of the coating to the substrate is greater than the cohesive strength of the microspheres from the foam.

To further assess the difference in terms of mechanical strength, micro-indentation tests were performed on the different top coatings produced. The force needed to penetrate the first 5 µm of the different coatings is gathered in **Table 3**. Except for the thin top coatings performed in Ar atmosphere where the underlying substrate is rapidly reached, the force required to penetrate the 5 µm increases with increasing the oxidation of the microparticles from the top coating. The micro-indentations

performed on the APS and EB-PVD YSZ coatings show that there is a significant difference between the mechanical strength of the standard TBCs and the Al slurry ones. As a matter of fact, the indentations in the plasma-sprayed coatings resulted in an average load that was 10 times higher (~200 mN) than the Al slurry coatings performed in synthetic air. The indentations performed on the EB-PVD coatings were even higher but showed a wide dispersion of the values due to the inherent heterogeneity of the surface of these columnar coatings.

Table 3 – Results of the micro-indentation tests with the average load ($F_{N,av}$) applied to penetrate 5 microns into the different coatings.

Atmosphere of heat treatment	**$F_{N,av}$ (mN)**	
	HS	DS
Ar	19.6 ± 5.1	21.3 ± 9.3
Switch 700°C	8.5 ± 0.7	9.6 ± 2.3
Switch 650°C	12.0 ± 1.7	12.6 ± 4.5
Synthetic air	17.6 ± 7.4	27.3 ± 4.5
Other standard thermal barrier coatings		
APS YSZ	201.3 ± 22.0	
EB-PVD YSZ	897.3 ± 229.0	

3.3. Thermal diffusivity

The thermal diffusivity of the top coatings was then calculated via laser-flash measurements of the complete system (substrate + aluminide + top coating) and the results are presented in **Figure 7**. All the coatings present thermal diffusivity values ranging between $0.8 \cdot 10^{-7}$ to $5.0 \cdot 10^{-7}$ $m^2.s^{-1}$ with trends that decrease as a function of the temperature. By comparing the two different types of microparticles, the thermal diffusivity of the HS microparticles -based coatings display higher thermal diffusivity than the DS ones with ranges going from $1.4 \cdot 10^{-7}$ to $5.0 \cdot 10^{-7}$ $m^2.s^{-1}$ and $0.8 \cdot 10^{-7}$ to $3.3 \cdot 10^{-7}$ $m^2.s^{-1}$ respectively. Independent of the type of microparticles (DS or

HS), the coatings that are the less oxidized (Ar) display the lowest thermal diffusivity and the top coatings that were heat treated in synthetic air present lower thermal diffusivities than the ones heat treated in Ar + air-650°C.

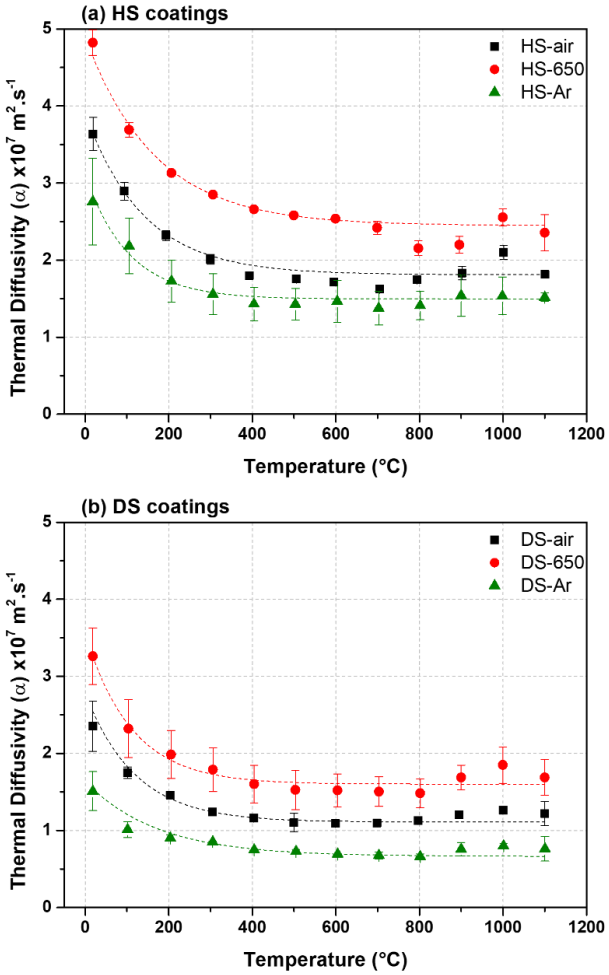

Figure 7 – Thermal diffusivity as a function of the temperature for (a) the HS foam coatings and (b) the HS foam coatings.

4. Discussion

As stated previously, the formation of the coatings is fully discussed in a previous work [2]. Therefore, the microstructural aspects of the coatings obtained in the different annealing conditions are only briefly presented in this work.

Annealing in a quasi-inert Ar atmosphere lead, for both HS and DS aluminium microparticles, to the fast consumption of the Al to form the aluminide coating and

the collapsing of the remaining emptied shells from the top coating due to a lack of strength of the oxide shells. This collapsing was explained in other studies to be due to the shrinkage of the thin alumina shells when γ-Al_2O_3 transform into the α-Al_2O_3 after exposure to temperatures above 1000°C [2,7,12,13]. The fact that the collapsing of the foam top coating was more obvious for the DS-Ar than for the HS-Ar sample is probably due to a thinner passive shell for the DS microparticles, (see **a** and **f** from **Figures 1** and **2**). The oxide shell thickness measured after the heat treatments for the DS particles is very thin (~0.2 μm) (**Figure 4**). Therefore, when Al starts to melt (around 660°C), the shells are not thick enough to avoid collapsing when the γ to α-Al_2O_3 transition occurs (see **Figure 2f**). The HS particles that display thicker shells, i.e. ~0.3 μm after the heat treatment, are able to withstand a bit more the transition and seem to keep a quasi-spherical shape (see cross sections on **Figure 2a**). In addition, the scratch tests performed on these thin coatings did not cause the detachment of the foam top coatings but rather resulted in the crushing of the hollow microspheres. As the coatings of this study are made of the agglomeration of small hollow oxide spheres on top of a hard aluminide coating, plastic deformation is supposed to be minimal as fracture should dominate the scratch response [11]. Therefore, as the strength of the oxide shells built under Ar atmosphere is very poor, the scratch only showed the brittleness and the poor cohesive strength of the foam coating. The micro-indentation tests performed on the DS-Ar and HS-Ar even showed higher value of the load needed to penetrate 5 microns (see **Table 3**) than the one of the coatings annealed in the other conditions. As the indenter rapidly reached the aluminide surface, it was not possible to properly measure the contribution of the top foam coating itself. Such poor mechanical strength was also observed in previous works and, is at the origin of the study that seek to improve the strength of the top foam [2].

The use of a heat treatment in synthetic air to improve the mechanical strength of the top foam coating resulted in the oxidation of the substrate that hampered the

diffusion of the aluminium from the microparticles to form the aluminide coating (**Figure 2e** and **2j**). However, such oxidation also resulted in an increase of the shell thickness of the microparticles (~0.5 μm and ~0.7 μm for DS and HS particles respectively) and a reduction of the collapsing of the emptied microspheres that led to thicker top foam coatings for the heat treatment in air compared than in Ar (see **Figures 3** and **4**). The scratch tests showed the good adhesion of the foam coating to the substrate despite the increase of the stiffness of the foam implied by the increase of the shell thickness and the sintering caused by the oxidation of the aluminium of the microparticles. This increase in hardness was highlighted by microindentation (see **Table 3**) as the HS-air and DS-air showed higher resistance than the coatings with introduction of the synthetic air during the heat treatment.

By introducing the synthetic air during the annealing, different improvements are achieved in comparison with the treatment performed under Ar or synthetic air only. Delaying the introduction of air from 700°C to 650°C and then to 600°C allowed longer exposition of the coating under the oxidation potential of the synthetic air and thus, allow the achievement of thicker oxide shells and thicker top coating than with a heat treatment under Ar only (see **Figures 3** and **4**). **With the introduction of air at 700°C**, almost no improvement was made on the thickness of the microsphere walls in comparison with the full Ar heat treatment, but the introduction of air allowed to slightly reduce the collapsing of the microspheres as the top coating achieved are thicker than the one under Ar atmosphere. **With the air introduced at 600°C**, the thickness of the shells and of the top coatings for both types of particles are greatly improved. However, similarly than with the heat treatment performed under air, the substrate oxidation hampers the formation of a homogeneous aluminide coating. It is only **with the introduction of air at 650°C** that a good compromise between the aluminide formation and the achievement of thick shells and top foam is found. The indentations performed on the different coatings (**Table 3**) also showed that the thickening of the oxide shells (**Figure 3**) lead to a greater resistance to the penetration

of the indent as time of exposure to the synthetic air increase, e.g. from 8.5-9.6 N with air introduced at 700°C to 12-12.6 N with air introduced at 650°C needed to penetrate 5 μm into the coating. However, when compared with bulk APS and EB-PVD YSZ coatings, the porous foam coating achieved in this study is still 20 to 75 less resistant than the previous two others. However, the porosity of the foam coatings cannot be compared with these bulk coatings that can reach, for instance, a maximum of ~25% porosity for the standard plasma sprayed YSZ coatings [9].

The high porosity of the foam coatings achieved in this study thus lead to great thermal insulation properties. The coatings heat treated in Ar present the lower thermal diffusivities since the shell of the microparticles that trap air is very thin. As a matter of fact, heat conduction is greater in alumina (λair ~5-35 W.m-1.K-1 at RT) than in the gas filled pores (λair ~0.025 W.m-1.K-1 at RT) and could decrease even further when the pores are smaller than the gas mean free path (typically pores ~1 μm) where the heat conduction of the gas falls below the conduction of the free gas to ~0.01 W.m-1.K-1 due to gas molecule-wall collisions (Knudsen conduction) [6-8]. However, the top coatings that were heat treated in air present lower thermal diffusivities than the one heat treated in Ar + air-650°C despite the thicker shells of the former. This could be explained by the fact that a thick thermal oxide grew at the interface between the top coating and the diffusion coating for the samples heat treated in synthetic air. As a matter of fact, the contribution of the oxide layer that was not considered in the multilayer calculation via the laser-flash technique was previously shown to be responsible for adding a non-negligible resistance to heat transport and hence, leading to an underestimation of the thermal diffusivity [9,10]. Moreover, the Al_HS coatings exhibit higher thermal diffusivity values than the Al_DS ones. This can be attributed to several factors that derive from the initial differences in particle size. Indeed, for the same coating thickness, the number of interfaces increases with decreasing the size of the particles. Therefore, and because interfaces are known to scatter the heat through ceramic coatings [9-11], the greater

the number of interfaces, the lower the thermal diffusivity. In addition, since the heat flow could also be enhanced when the ratio of material vs. void is more significant, the Al_HS particles whose particle shells are thicker than those of the Al_DS will lead to higher heat conduction. As also shown in another study, the thermal insulation potential of the foam coating is significant when compared with the standard APS and EB-PVD coatings that reaches thermal diffusivities between $1 \cdot 10^{-7}$ to $3 \cdot 10^{-7}$ $m^2.s^{-1}$ for APS YSZ and $3 \cdot 10^{-7}$ to $6 \cdot 10^{-7}$ $m^2.s^{-1}$ for EB-PVD YSZ coatings while the range of thermal diffusivity for the coatings in this study goes from $0.6 \cdot 10^{-7}$ to $5 \cdot 10^{-7}$ $m^2.s^{-1}$ [9,10].

5. Conclusions

- Great thermal insulation properties achieved for the foam coatings.
- Increase of the mechanical resistance with increasing the time of exposure to air during the heat treatment
- What about the relevance of the scratch test to perform adhesion assessment for such foam coatings?

ACKNOWLEDGEMENTS

The authors gratefully acknowledge…

REFERENCES

1. Pedraza, F.; Mollard, M.; Rannou, B.; Balmain, J.; Bouchaud, B.; Bonnet, G. Potential Thermal Barrier Coating Systems from Al Microparticles. Mechanisms of Coating Formation on Pure Nickel. *Materials Chemistry and Physics* **2012**, *134*, 700–705, doi:10.1016/j.matchemphys.2012.03.053.
2. Boissonnet, G.; Grégoire, B.; Bonnet, G.; Pedraza, F. Development of Thermal Barrier Coating Systems from Al Microparticles. Part I: Influence of Processing Conditions on the Mechanisms of Formation. *Surface and Coatings Technology* **2019**, *380*, doi:10.1016/j.surfcoat.2019.125085.

3. Galetz, M.C.; Montero, X.; Mollard, M.; Günthner, M.; Pedraza, F.; Schütze, M. The Role of Combustion Synthesis in the Formation of Slurry Aluminization. *Intermetallics* **2014**, *44*, 8–17, doi:10.1016/j.intermet.2013.08.002.
4. Montero, X.; Galetz, M.; Schütze, M. A Single Step Process to Form In-Situ an Alumina Foam/Aluminide TBC System for Alloys in Extreme Environments at High Temperatures. *Surface and Coatings Technology* **2011**, *206*, 1586–1594, doi:10.1016/j.surfcoat.2011.05.052.
5. Mollard, M.; Rannou, B.; Bouchaud, B.; Balmain, J.; Bonnet, G.; Pedraza, F. Comparative Degradation of Nickel Aluminized by Slurry and by Pack Cementation under Isothermal Conditions. *Corrosion Science* **2013**, *66*, 118–124, doi:10.1016/j.corsci.2012.09.009.
6. Brossard, M.; Bouchaud, B.; Pedraza, F. Influence of Water Vapour on the Oxidation Behaviour of a Conventional Aluminide and a New Thermal Barrier Coating System Sintered from a Slurry: Water Vapour Oxidation of Aluminide Coatings. *Materials and Corrosion* **2014**, *65*, 161–168, doi:10.1002/maco.201307106.
7. Kolarik, V.; Roussel, R.; Juez Lorenzo, M.; Fietzek, H. Factors Influencing the Formation of a Diffusion Zone and the Adherence of the Top Coat of High Temperature Coatings from Micro-Sized Spherical Aluminium Particles. *Materials at High Temperatures* **2012**, *29*, 89–94, doi:10.3184/096034012X13316583881350.
8. Pedraza, F.; Rannou, B.; Boissonnet, G.; Bouchaud, B.; Maache-Rezzoug, Z. Rheological Behaviour, Synthesis and Performance of Smart Thermal Barrier Coating Systems Based on Hollow Alumina. *MSCE* **2015**, *03*, 17–22, doi:10.4236/msce.2015.312004.
9. Boissonnet, G.; Bonnet, G.; Pasquet, A.; Bourhila, N.; Pedraza, F. Evolution of Thermal Insulation of Plasma-Sprayed Thermal Barrier Coating Systems with Exposure to High Temperature. *Journal of the European Ceramic Society* **2019**, *39*, 2111–2121, doi:10.1016/j.jeurceramsoc.2019.01.026.
10. Boissonnet, G.; Chalk, C.; Nicholls, J.R.; Bonnet, G.; Pedraza, F. Phase Stability and Thermal Insulation of YSZ and Erbia-Yttria Co-Doped Zirconia EB-PVD Thermal Barrier Coating Systems. *Surface and Coatings Technology* **2020**, *389*, 125566, doi:10.1016/j.surfcoat.2020.125566.
11. Bull, S.J.; Berasetegui, E.G. An Overview of the Potential of Quantitative Coating Adhesion Measurement by Scratch Testing. *Tribology International* **2006**, *39*, 99–114, doi:10.1016/j.triboint.2005.04.013.
12. Hasani, S.; Panjepour, M.; Shamanian, M. The Oxidation Mechanism of Pure Aluminum Powder Particles. *Oxid Met* **2012**, *78*, 179–195, doi:10.1007/s11085-012-9299-1.
13. Hasani, S.; Soleymani, A.P.; Panjepour, M.; Ghaei, A. A Tension Analysis During Oxidation of Pure Aluminum Powder Particles: Non-Isothermal Condition. *Oxid Met* **2014**, *82*, 209–224, doi:10.1007/s11085-014-9488-1.